Review Article | Experiment, Engineering, and Physics

https://doi.org/10.3348/kjr.2017.18.4.555
pISSN 1229-6929 · eISSN 2005-8330
Korean J Radiol 2017;18(4):555-569

Korean Journal of Radiology
KJR

Dual-Energy CT: New Horizon in Medical Imaging

Hyun Woo Goo, MD, PhD[1], Jin Mo Goo, MD, PhD[2]

[1]Department of Radiology and Research Institute of Radiology, Asan Medical Center, University of Ulsan College of Medicine, Seoul 05505, Korea; [2]Department of Radiology, Seoul National University College of Medicine, Seoul 03080, Korea

Dual-energy CT has remained underutilized over the past decade probably due to a cumbersome workflow issue and current technical limitations. Clinical radiologists should be made aware of the potential clinical benefits of dual-energy CT over single-energy CT. To accomplish this aim, the basic principle, current acquisition methods with advantages and disadvantages, and various material-specific imaging methods as clinical applications of dual-energy CT should be addressed in detail. Current dual-energy CT acquisition methods include dual tubes with or without beam filtration, rapid voltage switching, dual-layer detector, split filter technique, and sequential scanning. Dual-energy material-specific imaging methods include virtual monoenergetic or monochromatic imaging, effective atomic number map, virtual non-contrast or unenhanced imaging, virtual non-calcium imaging, iodine map, inhaled xenon map, uric acid imaging, automatic bone removal, and lung vessels analysis. In this review, we focus on dual-energy CT imaging including related issues of radiation exposure to patients, scanning and post-processing options, and potential clinical benefits mainly to improve the understanding of clinical radiologists and thus, expand the clinical use of dual-energy CT; in addition, we briefly describe the current technical limitations of dual-energy CT and the current developments of photon-counting detector.

Keywords: *Dual-energy CT; CT imaging techniques; Spectral CT; Virtual monoenergetic imaging; Effective atomic number; Material decomposition; Photon-counting detector*

INTRODUCTION

CT is a cross-sectional, high-resolution, three-dimensional diagnostic imaging modality that generally uses single-energy polychromatic X-rays. Its recently increased clinical utility is primarily attributed to significantly increased scan speed as a synergic effect of increased gantry rotation speed and increased longitudinal detector coverage, as well as the development of various radiation-lowering techniques for favorable patient risk-to-benefit ratio (1). In contrast, CT has an inherent limitation in soft tissue differentiation because the pixel value or CT number entirely depends on the linear attenuation coefficient (μ) which has considerable overlap between different body materials. The linear attenuation coefficient is a result of two physical interactions between X-ray photons, i.e., the sum of photoelectric absorption that is predominant under low energy and Compton scattering that is predominant under high energy. Compton scattering strongly depends on the electron density of the material. The photoelectric effect is proportional to the cube of the atomic number (Z) and inversely proportional to the cube of the incident photon energy (E). Only a few heavy atoms, such as calcium, iodine, barium, and xenon, having

Received January 28, 2017; accepted after revision February 23, 2017.

Corresponding author: Hyun Woo Goo, MD, PhD, Department of Radiology and Research Institute of Radiology, Asan Medical Center, University of Ulsan College of Medicine, 88 Olympic-ro 43-gil, Songpa-gu, Seoul 05505, Korea.
• Tel: (822) 3010-4388 • Fax: (822) 476-0090
• E-mail: hwgoo@amc.seoul.kr

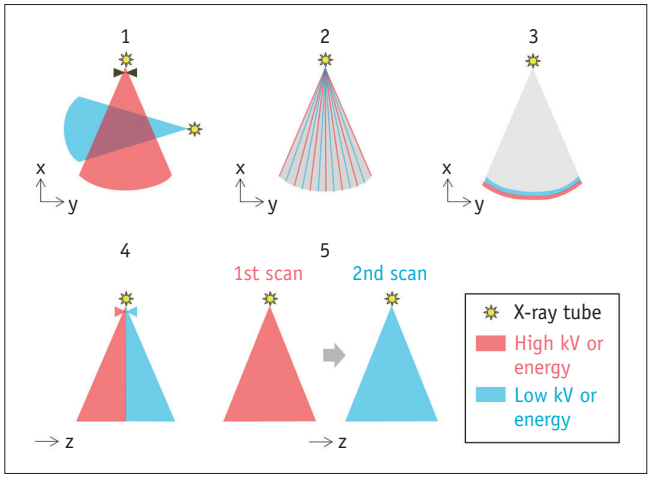

Fig. 1. Illustration of five different methods of dual-energy CT data acquisition. 1 = dual tubes with or without beam filtration, 2 = rapid voltage switching with single tube, 3 = dual-layer detector with single tube, 4 = single tube with split filter, 5 = single tube with sequential dual scans

strong photoelectric effect can be easily differentiated from other body tissue having similarly weak photoelectric effect. In this regard, dual-energy CT, introduced as a first-generation dual-source CT system in 2006, can improve material differentiation by using two different X-ray energy spectra (2). The concept of dual-energy CT was initially described in 1973 (3) and re-emerged in the field of clinical radiology with the recent technical developments in CT. The technical varieties and clinical applications of dual-energy CT are continuously expanding (4). Moreover, multi-energy CT using the so-called photon-counting detector technology is shedding new light on CT imaging (5). This review is targeted to clinical radiologists with an interest in dual-energy CT imaging, hence, the viewpoint may be slightly different from that for CT physicists or manufacturers involved in technical developments of dual-energy CT. Herein, we describe the current technical options for dual-

Table 1. Current Dual-Energy CT Acquisition Methods with Technical Specifications

CT Acquisition Methods	X-Ray Tube	Detectors	Gantry Rotation Time (s)	Temporal Offset (ms)	Z Coverage (cm)	Field of View (cm)	Contrast per Dose Efficiency†
Dual tubes with or without beam filtration*	Two X-ray tubes with or without tin filter, and with independently selected tube voltage pairs	Two sets of energy integrating detector	0.33, 0.28, 0.25*	83, 75, 66*	1.9, 3.8, 4.8*	26, 33, 35.5*	100%
Rapid voltage switching with single tube	One X-ray tube with rapidly changing tube voltage between 80 and 140 kVp	One set of energy integrating detector	0.5	0.5	4.0	50	35%
Dual-layer detector with single tube	One X-ray tube with 120 kVp	One set of dual-layer energy-resolving detector	0.27	Negligible	4.0	50	22–45%
Single tube with split filter	One X-ray tube with split gold/tin filter, and with 120 kVp	One set of energy integrating detector	0.28	280‡	3.8	50	Not available
Single tube with sequential dual scans	One X-ray tube; first at low kV, second at high kV	One set of energy integrating detector	0.27–0.28	> One scan time	4.0–16.0	50	70%

*Two X-ray tubes and two detector arrays almost orthogonally oriented each other in dual-source CT system; three values in gantry rotation time, temporal offset, z coverage, and field of view represent those for first, second, and third generations, respectively, †Relative contrast-to-noise ratio per radiation dose normalized to dual-source dual-energy technique (21), ‡Temporal offset probably caused by pitch factor limited to 0.5.

Korean Journal of Radiology
KJR

energy CT with their advantages and disadvantages, the diverse spectrum of clinical applications of dual-energy CT, and the current technical limitations and future directions of dual-energy CT.

Current Technical Options for Dual-Energy CT

We define the technical principles underlying the currently available dual-energy techniques to facilitate ease of understanding and avoid conceptual confusion. Five technical options are illustrated in Figure 1; and their technical specifications are summarized in Table 1.

Dual Tubes with or without Beam Filtration

This method requires a dual-source CT system in which each X-ray tube produces different X-ray energy spectra. The most striking advantage of this method is that the tube voltage, tube current, and filter are adjustable to maximize dual-energy spectral contrast and radiation dose efficiency based on the patients' body size and diagnostic purpose. Different combinations of tube voltages with or without a tin filter are available for the first (80 kVp/140 kVp), second (additionally available pairs: 80 kVp/140 Sn kVp, 100 kVp/140 Sn kVp), and third (additionally available pairs: 70 kVp/150 Sn kVp, 80 kVp/150 Sn kVp, 90 kVp/150 Sn kVp, 100 kVp/150 Sn kVp) generations of the dual-source CT system, with gradual increases in the magnitude of dual-energy spectral separation from the first to the third generation. Among these, the combination of 70 kVp and 150 kVp with a tin filter available in the third generation dual-source CT system currently provides the highest dual-energy spectral contrast and seems to be particularly useful in evaluating small body parts, such as the whole body of children and the extremities of adults and children. However, cross-scatter radiation inevitably degrades the dual-energy CT image quality due to the unique orthogonal geometry between the two tube-detector pairs; moreover, the adverse effect may not be completely eliminated despite the use of a small portion of detector elements to measure and correct the cross-scatter radiation. The angular offset (approximately 90° for the first generation, and 95° for the second and third generation) between the two tubes results in a small temporal difference that may be recognized as motion artifacts in and around rapidly moving structures, such as the heart. Projection-domain dual-energy processing is difficult to perform due to the temporal difference between the two projection data sets; therefore, an image-based algorithm is required for dual-energy image reconstruction in the method. Due to the smaller detector, the field of view (FOV) of dual-energy CT is limited to 26, 33, or 35 cm depending on the generation of dual-source CT system. Nonetheless, the target organ or structure is usually within the dual-energy FOV, and the anatomy outside the dual-energy FOV can be evaluated because the larger detector data is available for single-energy image reconstruction.

Rapid Voltage Switching with Single Tube

In this method, tube voltage is rapidly changed between 80 and 140 kVp, and the two projection data sets are collected separately for subsequent use in a projection-based dual-energy reconstruction algorithm. The rise and fall times required for voltage modulation limit the quality of two voltage-specific projection data; and reduced gantry rotation speed (0.5 second or longer) is required to allow dual-energy CT scanning. Slow gantry rotation introduces considerable motion artifacts that nullify the small temporal offset (0.5 ms) between the two X-ray energy spectra. Difference in photon output between high and low voltages is another critical problem of this method, leading to high radiation exposure to compensate for degraded image quality. Recently, this problem has been addressed by increasing the low-voltage exposure time ratio from 50 to 65%, but the dwell time ratio (65:35) cannot be further increased without increasing the angular mismatch between the two energy projections (6, 7). In addition, the reduced number of projections for each energy spectra may compromise the overall image quality. Other disadvantages include a limited dual-energy spectral contrast and non-availability of tube current modulation for radiation dose reduction. A potential benefit of projection-based algorithm, such as reduction of beam-hardening artifact and accurate CT densitometry, is not confirmed in this method (8, 9). Only 140 kVp images with high image noise are available for diagnostic imaging immediately after dual-energy scanning requiring additional reconstruction of virtual monoenergetic imaging, e.g., 70 keV imaging; this results in improved image quality for diagnostic imaging despite a minor practical limitation in workflow (Fig. 2).

Dual-Layer Detector with Single Tube

In this method, the unique dual-layer energy-resolving detector is used for dual-energy data acquisition. Polychromatic X-ray photons are generated by one tube;

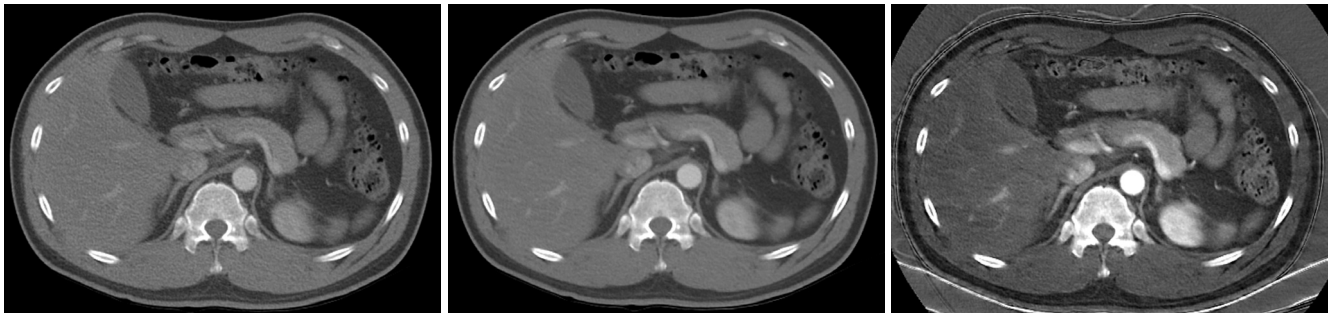

Fig. 2. Contrast-enhanced axial abdominal CT images using rapid voltage switching with single tube.
A. Image generated immediately after dual-energy scanning by using 140 kVp projections only shows high image noise. **B.** Virtual monoenergetic image at 70 keV showing improved image quality needs to be additionally reconstructed for diagnostic imaging. **C.** Iodine map demonstrates improved iodine contrast-to-noise ratio. Of note, patient skin, cloth, and CT table appear artifactually bright on iodine map.

thus, dual-energy scan is performed at a single fixed-tube voltage, generally 120 kVp, unlike other methods using two different tube voltages. The inner thin layer consisting of yttrium-based scintillator absorbs low-energy photons selectively, while the outer thick layer consisting of $Gd_2O_2S_2$ absorbs high-energy photons. Temporal difference between the dual-energy data is almost negligible. Projection-based algorithm used in the method has potential advantage over image-based algorithm, particularly in beam-hardening correction at the expense of a higher noise level for material decomposition images (7). Projection-based method generally involves difficult calibration process, scatter problem, and intense computation, as compared with the image-based approach (7). As an important merit in workflow, dual-energy evaluation can be performed retrospectively after CT scanning in all clinical cases, but at the expense of a relatively long dual-energy reconstruction time. Dual-energy scanning can be performed with full rotation speed (0.27 second) and full FOV (50 cm). However, the dual-energy spectral contrast is lower than that of dual tubes with beam filtration because the sensitivity profiles of the scintillator materials between the two layers are considerably overlapped. Disadvantages related to the complex detector design include a lower sensitivity to optical photons and cross-talk between the two detector layers (7). Further clinical investigation is required to fully define dual-energy performance.

Single Tube with Split Filter

In this method, a split filter is applied to a single X-ray tube at 120 kVp to obtain two separated but overlapped X-ray energy spectra (the so-called twin beam), limiting dual-energy spectral contrast to lower levels than that achieved by a combination of 80 and 140 kVp. The split filter consists of 0.05-mm thick gold filter to decrease X-ray photon energy and 0.6-mm thick tin filter to increase X-ray photon energy. As compared with the sequential dual-data acquisition method, this method enables dual-energy evaluation of enhanced or moving structures by minimizing the temporal difference between the two X-ray energy spectra equivalent to single gantry rotation time. Pitch factor is limited to 0.5 to maintain gapless imaging volume. Radiation dose is almost neutral to single-energy CT; however, greater X-ray output is necessary because the pre-filtration absorbs approximately two-thirds of the radiation.

Single Tube with Sequential Dual Scans

In this method, dual-energy CT data with spiral or sequential scanning are acquired simply twice sequentially with two different tube voltages, usually 80 and 140 kVp. Sophisticated CT hardware is not required, which may be regarded as a merit. However, the method is greatly limited by the greatest temporal difference between the two X-ray energy spectra precluding many dual-energy evaluations involved in contrast enhancement and moving body parts. As a result, its clinical application is restricted to unenhanced studies, such as kidney stone differentiation, gout, and metal artifact reduction in metal implants. This method uses an image-based dual-energy reconstruction algorithm; and radiation-lowering technique such as tube current modulation can be used.

Dual-Energy Applications

Dual-energy CT applications can largely be divided into exploration of material-nonspecific and material-specific energy-dependent information. Both evaluations can be qualitative or quantitative. The former includes virtual

Korean Journal of Radiology
KJR

monoenergetic imaging, effective atomic map, and electron density map. The latter includes material decomposition, material labeling, and material highlighting.

Virtual Monoenergetic or Monochromatic Imaging

Linear or nonlinear (combining high iodine contrast and low noise to provide optimal image contrast) blending of dual-energy CT data is a simple approach to generate CT images for routine diagnosis (Fig. 3A). Virtual monoenergetic images are synthesized by decomposing two basis materials, reconstructing the bone and water density map at the projection domain, and combining the mass density maps linearly at each energy; or generated simply by combining the low and high kVp CT images linearly at the image domain (9). Previously, uncompensated higher noise at lower keV image hampered the optimal use of virtual monoenergetic imaging for general contrast-enhanced CT exams (Fig. 3B) (9). In contrast, comparable or higher iodine contrast-to-noise ratio can be achieved in the recently introduced virtual monoenergetic imaging techniques with energy domain noise reduction, as compared with single-energy scan at optimal kVp and linearly-blended techniques (Fig. 3C) (10, 11). Energy domain noise reduction technique reduces image noise by exploiting information redundancy between low- and high-energy images with the same anatomic details (10). The benefits of the energy domain noise reduction technique

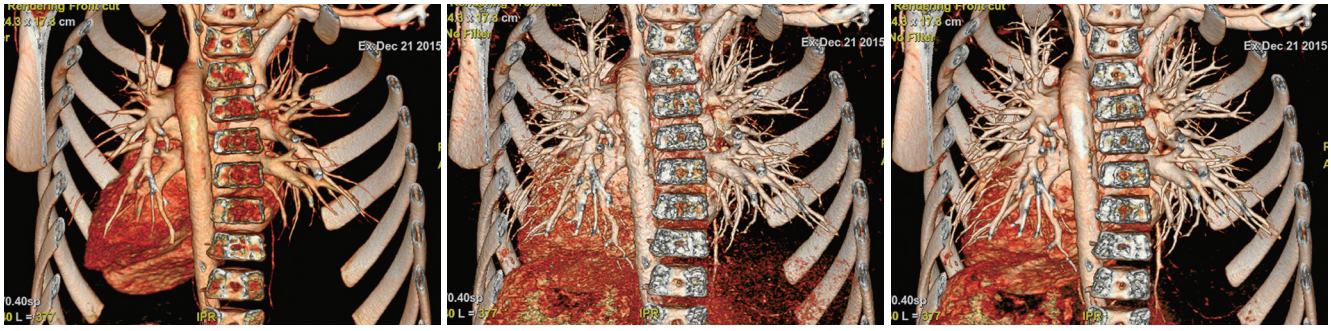

A B C

Fig. 3. Contrast-enhanced chest volume-rendered CT images with cropped posterior chest wall to unveil cardiovascular structures.
A, B. Compared with volume-rendered image reconstructed from linearly mixed dual-energy images with ratio of 0.8 **(A)**, volume-rendered 40 keV virtual monoenergetic image **(B)** shows further increase in cardiovascular opacification, but simultaneously increased noise compromises iodine contrast-to-noise ratio and image quality. **C.** On volume-rendered noise-optimized 40 keV virtual monoenergetic image, image noise reduction decoupled with increased iodine contrast leads to improved iodine contrast-to-noise ratio and image quality.

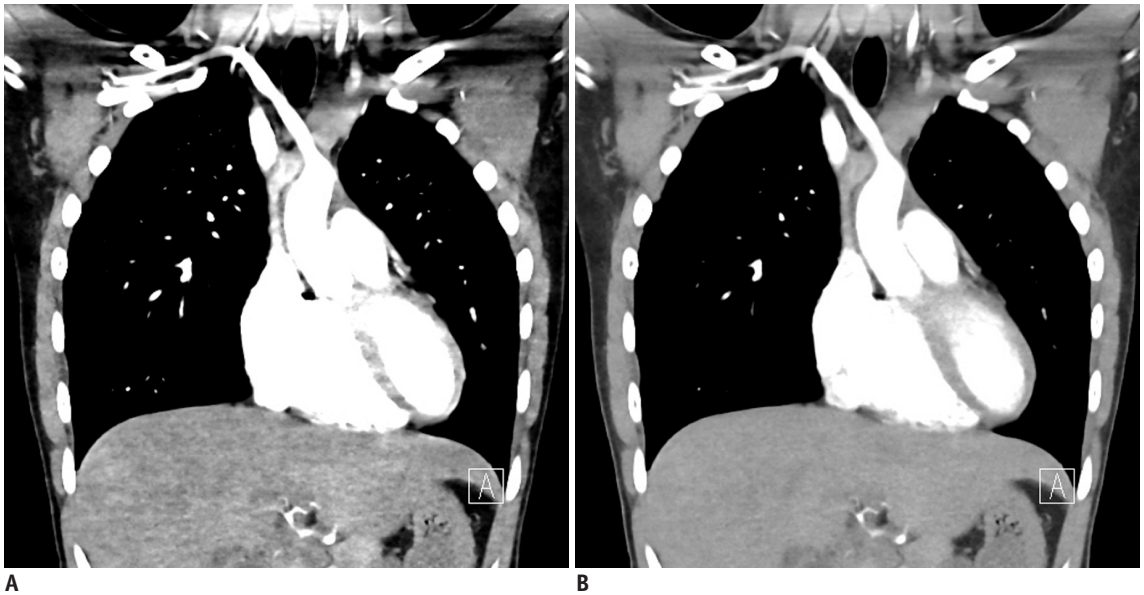

A B

Fig. 4. Coronal chest noise-optimized virtual monoenergetic dual-energy CT imaging.
Beam-hardening and/or photon starvation artifacts in thoracic inlet and shoulder pronounced in 40 keV image **(A)** are reduced in 60 keV images **(B)**. Because iodine contrast is progressively reduced at higher keV images, overall optimal image quality can be achieved around 60 keV depending on patients' size as well as body region.

include preserved spatial resolution and synergistic effect with spatial domain noise reduction technique, i.e., iterative reconstruction. The increased iodine contrast-to-noise ratio of noise-optimized virtual monoenergetic low keV images is useful to reduce the amount of intravenous iodine contrast agent, salvage enhanced CT studies with suboptimal enhancement, or increase small-vessel visibility (Fig. 3) (12). However, beam-hardening and/or photon-starvation artifacts at thick body regions, such as shoulder and pelvis, are still pronounced in noise-optimized low keV images (Fig. 4). It is difficult to compensate for photon-starvation artifacts with high keV images. In unenhanced brain CT, the image quality can be maximized at 65–75 keV images, as compared with single-energy 120 kV images (13). Materials can be qualitatively and graphically differentiated by spectral attenuation curve as a function of energy (Fig. 5) (9, 14). Metal artifacts can be reduced at high keV images (95–150 keV) at the expense of loss of iodine enhancement (Fig. 6) (9); whereas, iterative metal artifact reduction algorithm offers greater reduction of metal artifacts with relatively preserved iodine contrast and CT numbers than high keV images and the combination of the two provides an incremental benefit compared to both single methods (15).

Effective Atomic Number (Z_{eff}) Map and Electron Density (ρ_e) Map

Effective atomic number (Z_{eff}) and electron density (ρ_e) can be calculated from dual-energy CT data with small errors of 1.7 and 4.1%, respectively (16). Effective atomic number map is a quantitative approach in material differentiation

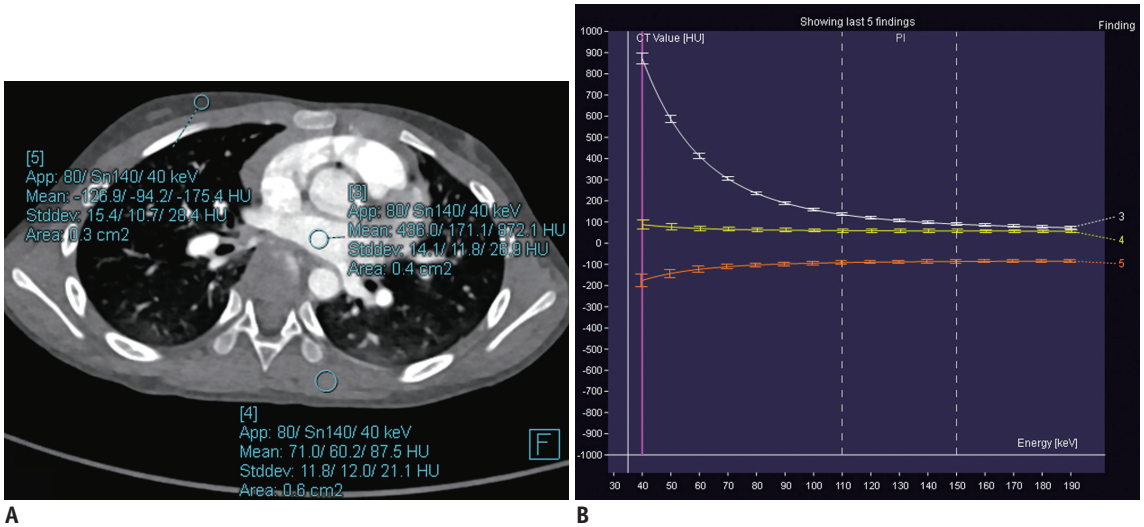

A B

Fig. 5. Contrast-enhanced axial chest virtual monoenergetic dual-energy CT imaging.
A. Three round regions of interest are placed in left atrium, back muscle, and subcutaneous fat in anterior chest wall, respectively, on axial chest CT image. **B.** Graph illustrating changes in CT value in three regions of interest as function of energy. Iodine in blood (white line) shows higher CT values at lower keV, while fat (orange line) reveals lower CT values at lower keV. In contrast, muscle (yellow line) demonstrates almost constant CT values in range of 40–190 keV.

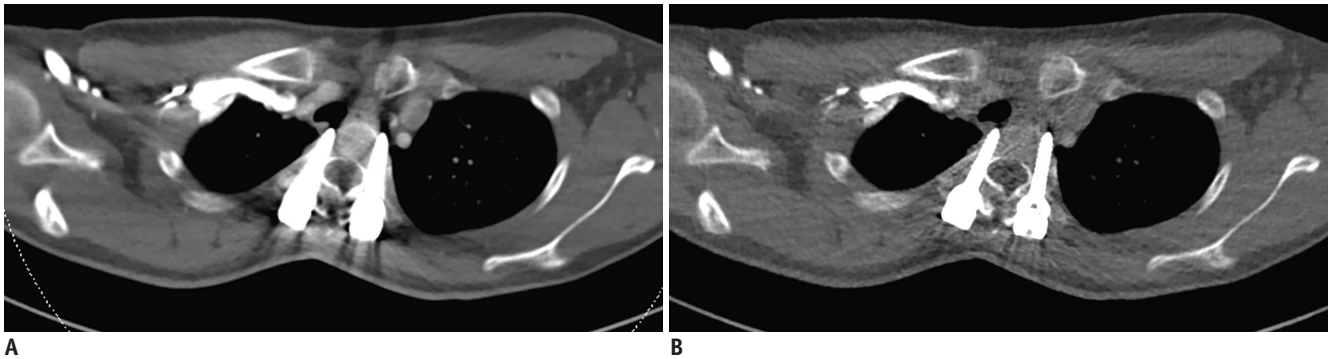

A B

Fig. 6. Contrast-enhanced axial chest dual-energy CT imaging with posterior spinal fixation for scoliosis.
A. Linearly mixed image with ratio of 0.4 shows beam-hardening artifacts caused by pedicle screws. **B.** Beam-hardening artifacts become less prominent on 130 keV image at expense of reduced iodine enhancement in vessels.

Korean Journal of Radiology
KJR

by analyzing attenuation changes as a function of energy. CT number of water is zero irrespective of X-ray energy and likewise, Z_{eff} of water is approximately 7.4–7.5. Of interest, lung perfusion defects caused by pulmonary embolism can be distinguished from the normally perfused lung more clearly on effective atomic number map than on iodine map (Fig. 7).

Material Decomposition

In the three-material decomposition used for a dual-source system in the image domain, iodine map is generated from the iodine concentration quantified in each voxel based on two basis materials, fat and soft tissue; and virtual non-contrast (VNC) or unenhanced image is produced by subtracting the iodine map from the dual-energy enhanced CT image. In contrast, the two-material, water and iodine, decomposition is used for a single-source system in the projection domain.

Virtual Non-Contrast or Unenhanced Imaging and Iodine Map

In all body regions, VNC imaging may replace a pre-contrast scan and substantially reduce radiation exposure, which is particularly useful in children. For example, Chen et al. (17) reported that split-bolus dual-energy CT urography allowed 56.4% reduction of radiation dose by eliminating the need for a pre-contrast scan. However, the size of calcification tends to be smaller on VNC imaging, as compared with that on true non-contrast imaging (14, 17-20), and tiny calcifications or calcified stones may be overlooked on VNC imaging. On the contrary, incompletely removed iodine areas result in false positive findings (17). Usually, CT numbers of soft tissues are slightly overestimated on VNC imaging (14, 17, 18). The noise levels of the VNC images as well as iodine maps are strongly correlated with the inversion of the dual-energy ratio, emphasizing the importance of spectral separation (7, 21). Furthermore, greater spectral separation reduces the erroneous discrimination between iodine and calcium on VNC images.

In the abdominal region, VNC images allow better visualization of isodense cholesterol gallstones with accentuated contrast chiefly due to increased attenuation value of fat at higher tube voltage (20). Liver iron overload may be quantified by using an iron-specific three-material decomposition algorithm with similar diagnostic performance to MRI (22) and, therefore, it may be used as an alternative method when MRI is not available or contraindicated.

Similarly, synovial hemosiderin deposits can be identified on dual-energy CT in patients with pigmented villonodular synovitis (23). As in intravenously enhanced CT, VNC imaging may be applied to CT arthrography in the musculoskeletal region (23). In the musculoskeletal region, virtual non-calcium imaging may be used to evaluate the bone marrow that is beyond the scope of CT evaluation.

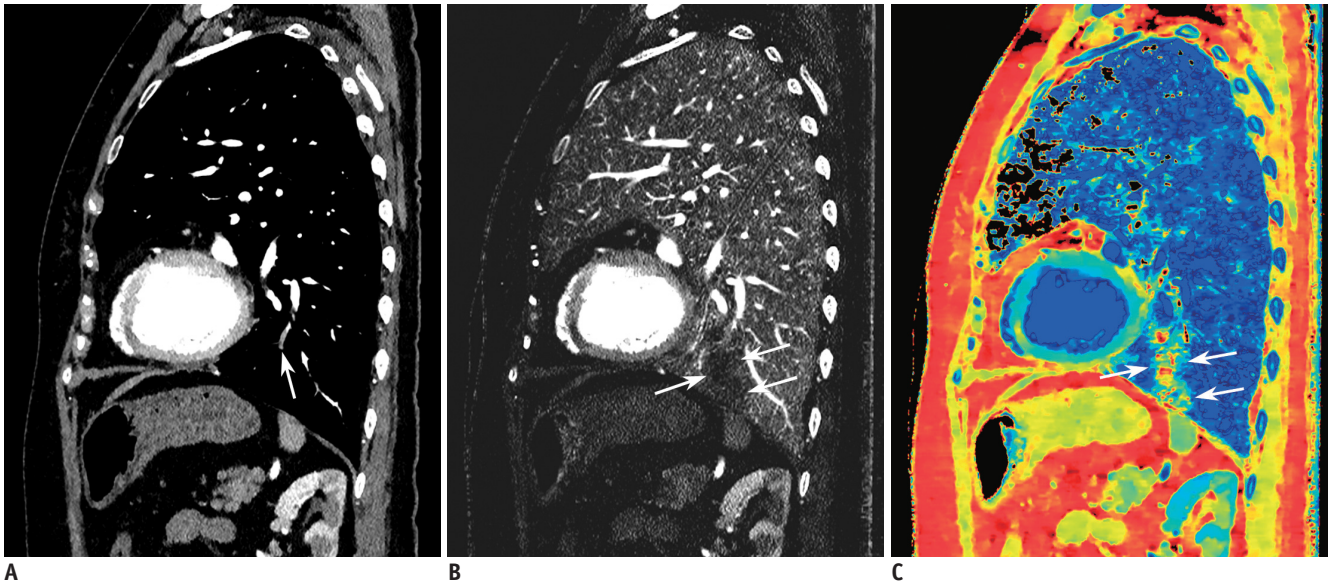

Fig. 7. Contrast-enhanced sagittal chest dual-energy CT imaging acquired with dual-layer detector technique.
A. 70 keV image reveals subsegmental embolus (arrow) in anterior basal segment of left lower lobe. **B, C.** Wedge-shaped perfusion defect (arrows) is seen on iodine map **(B)** and more conspicuously on effective atomic number map **(C)**.

Virtual non-calcium imaging subtracts calcium from cancellous bone and allows detection of acute traumatic bone marrow lesions including occult fractures and bone bruises, which cannot be clearly visualized on single-energy CT (23-25). Diagnostic performance of virtual non-calcium imaging tends to be better for small appendicular bones than axial skeletons. Adjustment of material decomposition ratio (*r*) is necessary for different tube voltage settings (1.45 for 80 and 140 kVp; 1.3 for 100 and 140 kVp) to eliminate bone mineral completely. Nevertheless, virtual non-calcium imaging is limited in evaluating bone marrow alterations close to the cortical bone or in sclerotic bone. In addition, false-positive results may occur due to the presence of normal red marrow, and other pathologies,

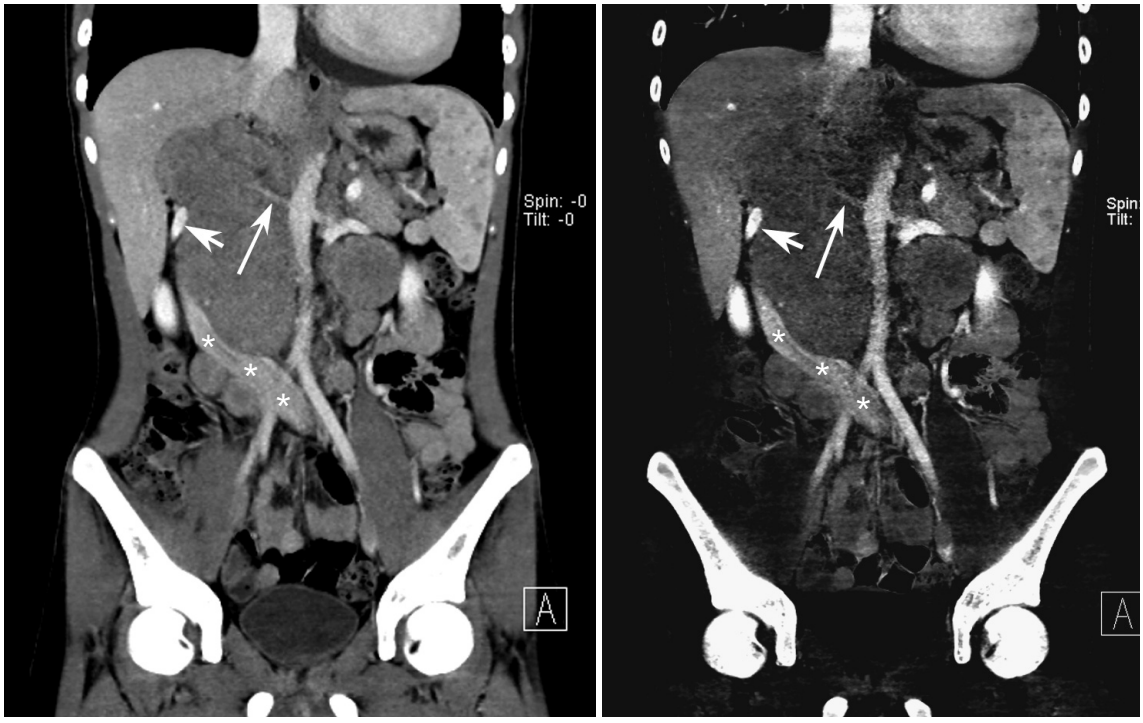

A B

Fig. 8. Coronal abdominopelvic dual-energy CT imaging in patient with Hodgkin lymphoma.
A, B. Linearly mixed image, iodine map. Right renal artery (long arrows), left renal vein (short arrows), inferior vena cava (asterisks) are displaced or encased by extensive, necrotic retroperitoneal lymphadenopathy. Lymphadenopathy shows subtle peripheral enhancement on iodine map **(B)**. Multiple hypodense small nodules are noted in spleen.

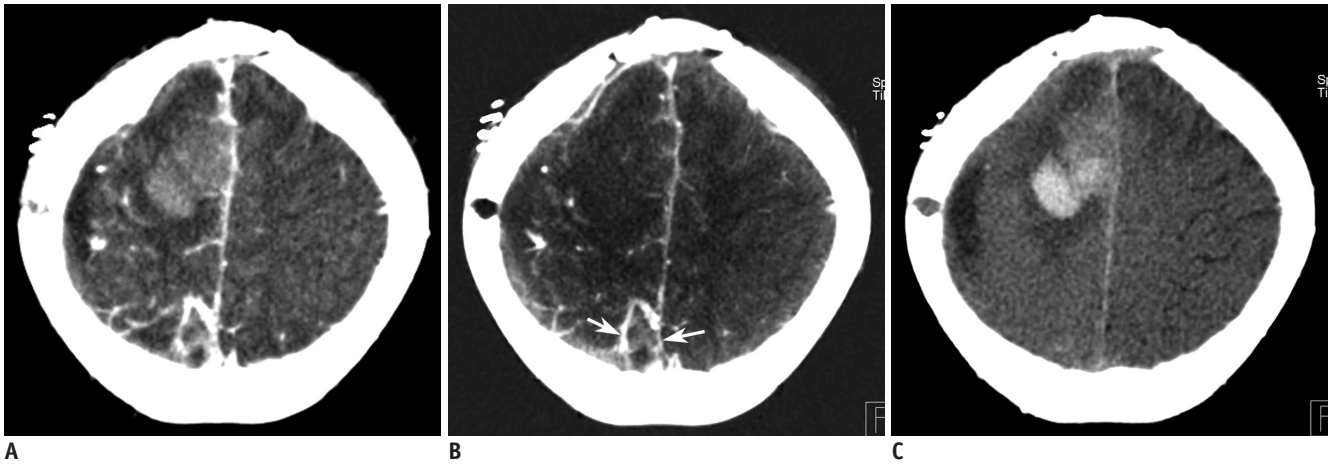

A B C

Fig. 9. Axial brain dual-energy CT imaging in patient with recurrent primitive neuroectodermal tumor.
A-C. Linearly mixed image, iodine map, virtual non-contrast image. Larger anterior hyperdense lesion, pure intracerebral hemorrhage, shows no enhancement on iodine map **(B)** and hyperdensity suggesting recent hemorrhage on virtual non-contrast image **(C)**. In contrast, smaller heterogenous lesion (arrows) reveals enhancing areas suggesting viable tumor on iodine map **(B)**.

Korean Journal of Radiology
KJR

such as osteonecrosis or degenerative changes, may mimic post-traumatic bone marrow lesions. A combined review of gray-scale images and color-coded images can facilitate the identification of small attenuation changes within the bone marrow (23-25). Of note, automatic color-coded bone marrow segmentation is incomplete, especially in the head region.

In the breast region, a color-coded map of unenhanced dual-energy CT may be used to depict silicone breast implant leaks from normal surrounding soft tissue with similar CT numbers due to the large differences in atomic numbers between the two (5).

Using contrast-enhanced dual energy CT data in all body regions, iodine map specifically shows iodine distribution in tissues with improved iodine contrast-to-noise ratio, but the bone and calcium are also included in the map (Figs. 8, 9). In the thoracic region, dual-energy lung parenchymal iodine or pulmonary blood volume (PBV) map, as a surrogate of lung perfusion, is mainly used to improve the diagnosis of pulmonary thromboembolism. By this method, characteristically wedge-shaped iodine-deficient lung lesions are detected, which are not apparent on conventional pulmonary CT angiography (Fig. 7) (26-28). In pulmonary thromboembolism, dual-phase dual-energy PBV map can be used to differentiate between acute and chronic phases by identifying delayed systemic collateral flow at the expense of higher radiation dose (29). Dual-energy PBV map can demonstrate that endothelial dysfunction represented with hypoxic peripheral arteriolar vasoconstriction is reversible after administration of oral sildenafil, supported by reduced PBV coefficients of variation due to lung perfusion heterogeneity, in smoking-associated emphysema (30).

In all body regions, due to improved lesion-to-background contrast, enhancing lesions or vessels are more conspicuous on the iodine map (Fig. 8). Iodine map is helpful not only to distinguish a particularly hyperdense, cystic lesion or hematoma from enhancing lesion, but also to clearly delineate the extent of bowel ischemia (14, 18, 25); in addition, malignant tumors may be more accurately differentiated from benign tumors based on the degree of iodine enhancement (19). Treatment response may be assessed quantitatively by measuring the iodine concentration in enhancing tumors in oncologic patients (14, 18, 28, 31).

In the head region, dual-energy iodine map is useful for differentiating between tumor bleeding and pure intracerebral hemorrhage (Fig. 9) or between contrast extravasation and intracerebral hemorrhage after intra-arterial revascularization in patients with acute ischemic stroke (32, 33).

In the cardiovascular region, static dual-energy stress myocardial perfusion CT is more useful than coronary CT angiography for the detection of hemodynamically significant coronary artery stenosis by providing myocardial iodine distribution during the early arterial phase (25, 34). In cardioembolic stroke, dual-energy cardiac CT with dual-phase (arterial and 3 minutes delayed) intravenous injection of contrast agent can be used to accurately differentiate between left atrial appendage thrombi and circulatory stasis (35). Iodine map increases confidence in detecting endoleaks after aortic stent graft placement (36).

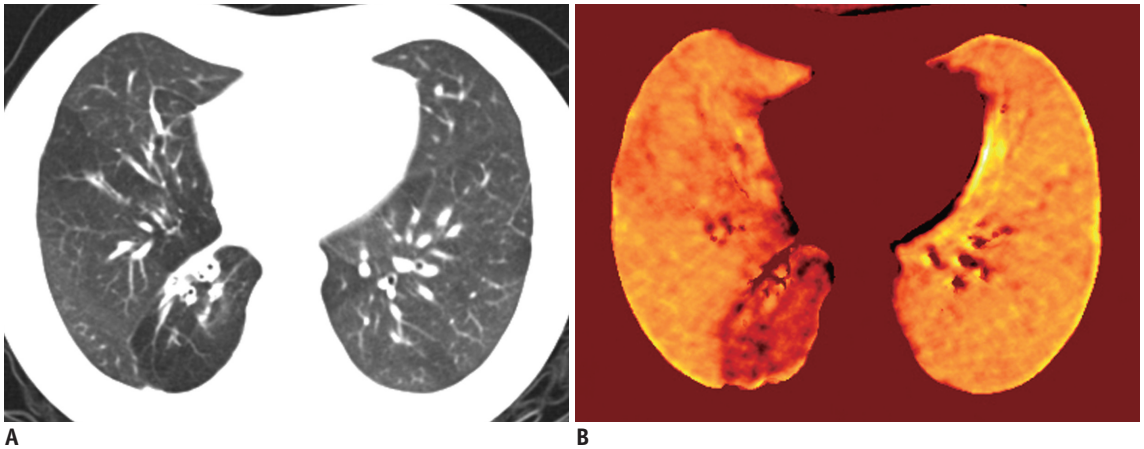

A B

Fig. 10. Axial chest xenon-inhaled dual-energy CT imaging in patient with post-infectious bronchiolitis obliterans.
A. Linearly mixed image shows bronchial wall thickenings and mosaic lung hyperlucency in right middle and lower lobes. Collapse of anterior basal segment of right lower lobe is also noted. **B.** Xenon map demonstrates severely reduced xenon enhancement in right lower lobe and mildly, heterogeneously decreased xenon enhancement in right middle lobe.

Lung Ventilation Map

Recently, xenon gas (atomic number 54) has been used for inhalation contrast agent for dual energy lung CT (37-47). Volumetric whole lung or dynamic focal lung scan protocol can be used during the xenon wash-in and wash-out periods (46). Xenon-inhaled dual-energy CT has been applied to various pulmonary diseases including chronic obstructive pulmonary disease (39, 47, 48), asthma (40-42), bronchiolitis obliterans (Fig. 10) (43), and bronchial atresia (37). Due to the anesthetic effect caused by increased blood xenon concentration, single inspiration technique of high-concentration xenon gas (45) or alternative use of krypton gas having no anesthetic effect (48, 49) is suggested. Lung density enhancement by krypton gas inhalation is lower than that by xenon gas inhalation (48). As in radionuclide ventilation-perfusion scans, dual-energy CT may be used to depict ventilation-perfusion mismatch specifically caused by pulmonary embolism (46, 49).

Material Differentiation or Labeling

In material differentiation or labeling, two materials with different dual-energy slopes caused by different photoelectric effects can be differentiated by using a pre-defined separation line.

Urinary Stone Differentiation

In nephrolithiasis, dual-energy CT can be used to reliably distinguish uric acid-containing stones from calcium-containing stones because the former consists of materials with significantly smaller atomic numbers than the latter (25). Dual-energy CT also can differentiate different types of non-uric acid calculi (50, 51).

Gout Imaging

Dual-energy CT can differentiate monosodium urate crystals from calcium-containing compounds within joints and periarticular soft tissues such as tendons with a sensitivity of 87% (95% confidence interval, 0.79–0.93) and a specificity of 84% (0.75–0.90) in a meta-analysis (Fig. 11) (25). In gout, dual-energy CT is particularly useful for cases with unusual locations, negative or inconclusive arthrocentesis, and other concomitant arthropathies, and evaluating total gout burden and treatment-response (23). For complete evaluation, the use of a standardized 4-limb dual-energy CT is suggested. Early crystals below threshold density for inclusion may result in false negative interpretations, while various artifacts can result in false positives (52).

Dual-Energy Bone Removal

Spectral information obtained with dual-energy CT can be

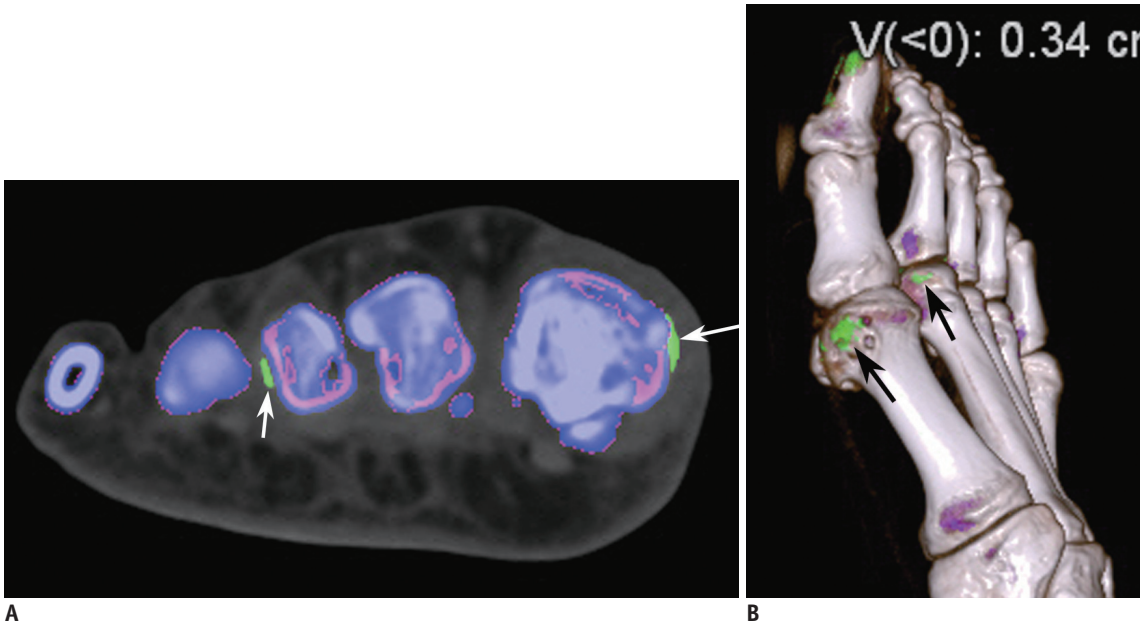

Fig. 11. Dual-energy CT imaging of right foot in patient with gout.
Color-coded map **(A)** and volume-rendered image **(B)** show periarticular green foci (arrows) suggesting monosodium urate deposits and associated soft tissue swelling. False-positive artifacts are noted in typical location around nail bed and skin of great toe on volume-rendered image **(B)**.

Korean Journal of Radiology
KJR

used to separate iodine from bone in CT angiography (Fig. 12). For whole-body CT angiography, dual-energy automatic bone removal offers significantly less errors in bone segmentation than threshold-based single-energy technique at equivalent radiation exposure and postprocessing time (53). The small errors in dual-energy bone removal can be minimized with greater spectral separation or higher dual-energy ratio of dual-energy CT data. Nevertheless, the quality of dual-energy bone removal is often inferior to that of subtraction technique using pre- and post-contrast scans.

Lung Vessels Analysis

The lung vessels analysis tool can be used to distinguish enhanced lung vessels from unenhanced lung vessels based on different slopes between the two on the dual-energy plot, irrespective of the vessel diameter (Fig. 13A) (46, 54). As a result, dual-energy lung vessels analysis improves the detection of small peripheral pulmonary embolism (54). However, the ability to correctly identify peripheral pulmonary embolism may be compromised by insufficient pulmonary arterial enhancement (Fig. 13B).

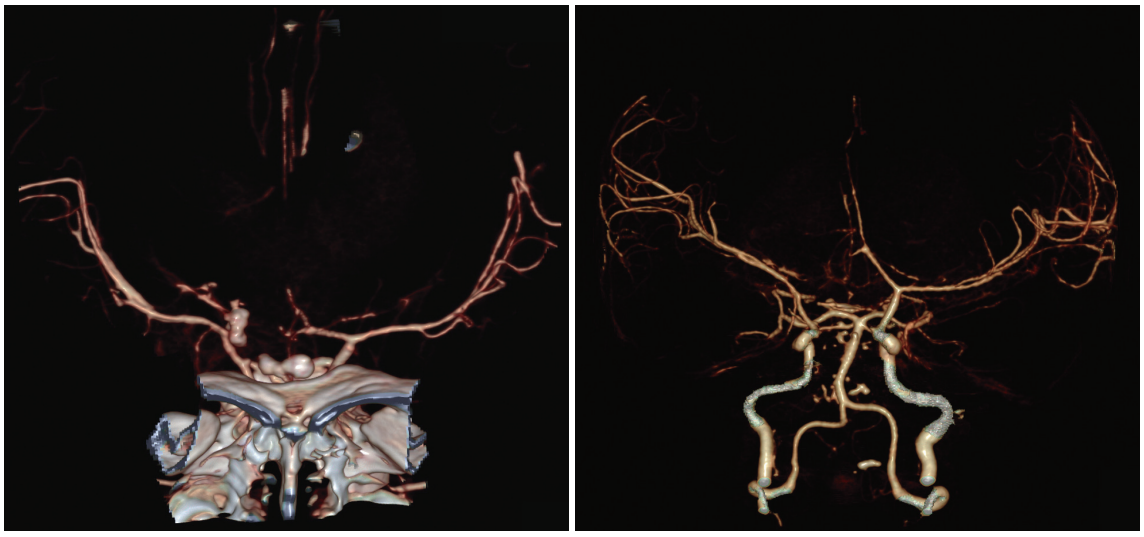

Fig. 12. Head CT angiographic volume-rendered imaging.
A. Three-dimensional dual-energy angiographic image after automatic dual-energy bone removal shows residual bone at skull base due to incomplete dual-energy iodine-bone separation. **B.** Three-dimensional dual-energy angiographic image after detailed manual bone removal improves quality of head angiography but is time-consuming.

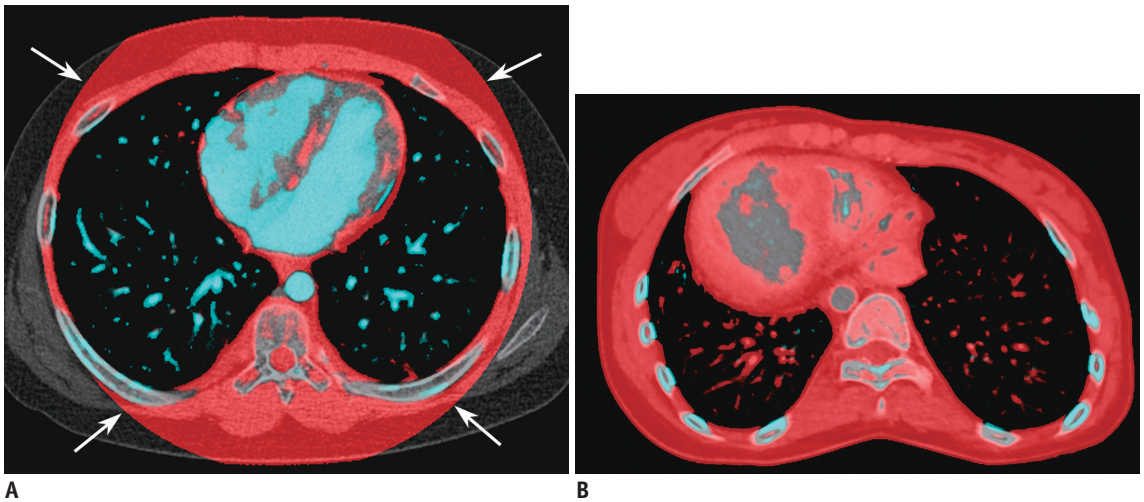

Fig. 13. Dual-energy chest CT imaging demonstrating lung vessels analysis.
A. Axial image with lung vessels analysis shows normal enhancing pulmonary vessels in light blue in both lungs and limited dual-energy field of view (arrows) typically seen in dual-energy technique using dual X-ray tubes. **B.** In patient with dextrocaria, pulmonary atresia, ventricular septal defect, right aortic arch, and Eisenmenger syndrome, unobstructed pulmonary vessels in both lungs are red, secondary to very slow pulmonary circulation.

Material Highlighting

Compared with single energy CT, dual-energy CT can improve the visualization of tendons and ligaments in the extremities by using the differences in atomic numbers between these structures and surrounding tissues, such as bone and fat (23, 25). As a result, abnormalities in large tendons and ligaments, such as avulsion, atrophy, compression, and thickening, can be better visualized.

Current Technical Limitations and Future Directions

In most dual-energy approaches available for current CT systems, motion artifacts and beam-hardening artifacts may deteriorate the image quality and need to be reduced (Fig. 14) (28, 46, 52). As in virtual monoenergetic imaging, further noise optimization is necessary for material decomposition images to improve their image quality in all dual-energy approaches. Development of more versatile dual-energy application algorithms is required to expand the clinical utility of dual-energy CT imaging. Imperfect bone or calcium segmentation or removal needs to be improved (Fig. 12A). Workflow issues including difficulties in CT scheduling, increased reconstruction time, increased number of images, and increased interpretation time, substantially increase the radiologists' workload and hinder the use of dual-energy CT imaging in daily routine (28).

In a photon-counting detector CT using cadmium-based semiconductors (CdTe or CdZnTe), single X-ray energy spectrum simultaneously acquired at a fixed tube voltage can be split into more than two photon energy bins, and is expected to be a promising future solution to overcome limitations of current CT imaging techniques including dual-energy scanning. In an optimized system, it has potential to not only eliminate electronic noise and misregistration between different energy bins, but also provide higher contrast-to-noise ratio, higher spatial resolution, higher radiation dose efficiency, and better spectral information (7, 55, 56). Also, a photon-counting detector is inherently suitable for projection-based material decomposition requiring perfectly registered X-ray spectra as in a dual-layer detector (7).

A photon-counting detector CT has several challenges including pulse pile-up, charge sharing, K-escape, Compton scattering, and charge trapping and causes non-ideal detector responses and data overlap in energy bins and eventually degrades the energy resolution of the CT system (7, 56). For example, the pulse pile-up effect that occurs in high tube currents when two or more photons are detected as one higher-energy photon due to their proximity in time, is regarded as one of challenges of photon-counting detector for clinical whole-body CT scanning requiring sufficiently high photon flux to provide high image quality. The charge sharing effect occurs due to incorrect detection of a photon by neighboring detector pixels at lower energy levels and occurs predominantly at very low tube current

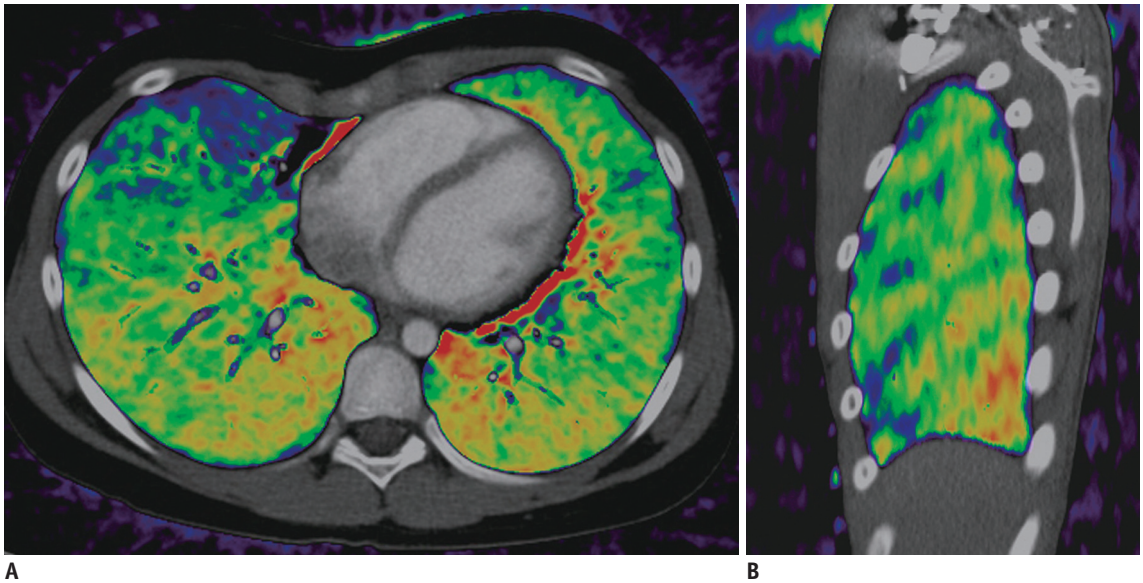

A B

Fig. 14. Dual-energy pulmonary blood volume map demonstrating cardiac motion and beam-hardening artifacts.
A. On axial pulmonary blood volume map, cardiac motion artifacts appear as red color areas around heart as well as blue areas in right middle lobe. **B.** On sagittal pulmonary blood volume map, beam-hardening artifacts appear as pattern of oblique stripes parallel to ribs.

Korean Journal of Radiology
KJR

settings in contrast to the pulse pile-up effect.

Initial phantom and human studies on photon-counting detector in abdominal CT (56) and whole-body CT (57) have been performed using a prototype built on the platform of a second-generation dual-source CT system. This facilitates direct comparison of imaging performance between an energy-integrating detector and a photon-counting detector. In these studies, the photon-counting detector showed comparable image quality to the conventional energy-integrating detector (56, 57). For the photon-counting detector, the pulse pile-up effect of high photon flux was negligible and loss of spatial resolution caused by charge sharing and K-escape did not occur (57). In addition, the photon-counting detector could provide multi-energy and material-specific information (56, 57). Imaging performance is anticipated to be continuously improved by tailoring and optimizing calibration, artifact correction algorithms, and dual- or multi-energy application algorithms for photon-counting detector in the near future.

CONCLUSION

Dual-energy CT enhances the diagnostic performance and confidence of CT by increasing iodine contrast-to-noise ratio, decreasing metal or beam-hardening artifacts, and providing material-specific information. In addition, patient safety is increased by the reduction of required contrast agent and by omitting true unenhanced CT. Radiologists should explore the various clinical benefits of dual-energy CT, an emerging technology in medical imaging.

REFERENCES

1. Goo HW. CT radiation dose optimization and estimation: an update for radiologists. *Korean J Radiol* 2012;13:1-11
2. Johnson TR, Krauss B, Sedlmair M, Grasruck M, Bruder H, Morhard D, et al. Material differentiation by dual energy CT: initial experience. *Eur Radiol* 2007;17:1510-1517
3. Hounsfield GN. Computerized transverse axial scanning (tomography). 1. Description of system. *Br J Radiol* 1973;46:1016-1022
4. Johnson TR. Dual-energy CT: general principles. *AJR Am J Roentgenol* 2012;199(5 Suppl):S3-S8
5. McCollough CH, Leng S, Yu L, Fletcher JG. Dual- and multi-energy CT: principles, technical approaches, and clinical applications. *Radiology* 2015;276:637-653
6. Maturen KE, Kaza RK, Liu PS, Quint LE, Khalatbari SH, Platt JF. "Sweet spot" for endoleak detection: optimizing contrast to noise using low keV reconstructions from fast-switch kVp dual-energy CT. *J Comput Assist Tomogr* 2012;36:83-87
7. Faby S, Kuchenbecker S, Sawall S, Simons D, Schlemmer HP, Lell M, et al. Performance of today's dual energy CT and future multi energy CT in virtual non-contrast imaging and in iodine quantification: a simulation study. *Med Phys* 2015;42:4349-4366
8. Mileto A, Barina A, Marin D, Stinnett SS, Roy Choudhury K, Wilson JM, et al. Virtual monochromatic images from dual-energy multidetector CT: variance in CT numbers from the same lesion between single-source projection-based and dual-source image-based implementations. *Radiology* 2016;279:269-277
9. Yu L, Leng S, McCollough CH. Dual-energy CT-based monochromatic imaging. *AJR Am J Roentgenol* 2012;199(5 Suppl):S9-S15
10. Leng S, Yu L, Fletcher JG, McCollough CH. Maximizing iodine contrast-to-noise ratios in abdominal CT imaging through use of energy domain noise reduction and virtual monoenergetic dual-energy CT. *Radiology* 2015;276:562-570
11. Albrecht MH, Trommer J, Wichmann JL, Scholtz JE, Martin SS, Lehnert T, et al. Comprehensive comparison of virtual monoenergetic and linearly blended reconstruction techniques in third-generation dual-source dual-energy computed tomography angiography of the thorax and abdomen. *Invest Radiol* 2016;51:582-590
12. Wichmann JL, Gillott MR, De Cecco CN, Mangold S, Varga-Szemes A, Yamada R, et al. Dual-energy computed tomography angiography of the lower extremity runoff: impact of noise-optimized virtual monochromatic imaging on image quality and diagnostic accuracy. *Invest Radiol* 2016;51:139-146
13. Pomerantz SR, Kamalian S, Zhang D, Gupta R, Rapalino O, Sahani DV, et al. Virtual monochromatic reconstruction of dual-energy unenhanced head CT at 65-75 keV maximizes image quality compared with conventional polychromatic CT. *Radiology* 2013;266:318-325
14. Agrawal MD, Pinho DF, Kulkarni NM, Hahn PF, Guimaraes AR, Sahani DV. Oncologic applications of dual-energy CT in the abdomen. *Radiographics* 2014;34:589-612
15. Bongers MN, Schabel C, Thomas C, Raupach R, Notohamiprodjo M, Nikolaou K, et al. Comparison and combination of dual-energy- and iterative-based metal artefact reduction on hip prosthesis and dental implants. *PLoS One* 2015;10:e0143584
16. Garcia LI, Azorin JF, Almansa JF. A new method to measure electron density and effective atomic number using dual-energy CT images. *Phys Med Biol* 2016;61:265-279
17. Chen CY, Hsu JS, Jaw TS, Shih MC, Lee LJ, Tsai TH, et al. Split-bolus portal venous phase dual-energy CT urography: protocol design, image quality, and dose reduction. *AJR Am J Roentgenol* 2015;205:W492-W501
18. De Cecco CN, Darnell A, Rengo M, Muscogiuri G, Bellini D, Ayuso C, et al. Dual-energy CT: oncologic applications. *AJR Am J Roentgenol* 2012;199(5 Suppl):S98-S105
19. Chae EJ, Song JW, Seo JB, Krauss B, Jang YM, Song KS. Clinical utility of dual-energy CT in the evaluation of solitary pulmonary nodules: initial experience. *Radiology*

2008;249:671-681
20. Lee HA, Lee YH, Yoon KH, Bang DH, Park DE. Comparison of virtual unenhanced images derived from dual-energy CT with true unenhanced images in evaluation of gallstone disease. *AJR Am J Roentgenol* 2016;206:74-80
21. Krauss B, Grant KL, Schmidt BT, Flohr TG. The importance of spectral separation: an assessment of dual-energy spectral separation for quantitative ability and dose efficiency. *Invest Radiol* 2015;50:114-118
22. Luo XF, Xie XQ, Cheng S, Yang Y, Yan J, Zhang H, et al. Dual-energy CT for patients suspected of having liver iron overload: can virtual iron content imaging accurately quantify liver iron content? *Radiology* 2015;277:95-103
23. Omoumi P, Verdun FR, Guggenberger R, Andreisek G, Becce F. Dual-energy CT: basic principles, technical approaches, and applications in musculoskeletal imaging (part 2). *Semin Musculoskelet Radiol* 2015;19:438-445
24. Pache G, Krauss B, Strohm P, Saueressig U, Blanke P, Bulla S, et al. Dual-energy CT virtual noncalcium technique: detecting posttraumatic bone marrow lesions--feasibility study. *Radiology* 2010;256:617-624
25. McLaughlin PD, Mallinson P, Lourenco P, Nicolaou S. Dual-energy computed tomography: advantages in the acute setting. *Radiol Clin North Am* 2015;53:619-638, vii
26. Thieme SF, Johnson TR, Lee C, McWilliams J, Becker CR, Reiser MF, et al. Dual-energy CT for the assessment of contrast material distribution in the pulmonary parenchyma. *AJR Am J Roentgenol* 2009;193:144-149
27. Goo HW. Initial experience of dual-energy lung perfusion CT using a dual-source CT system in children. *Pediatr Radiol* 2010;40:1536-1544
28. Otrakji A, Digumarthy SR, Lo Gullo R, Flores EJ, Shepard JA, Kalra MK. Dual-energy CT: spectrum of thoracic abnormalities. *Radiographics* 2016;36:38-52
29. Hong YJ, Kim JY, Choe KO, Hur J, Lee HJ, Choi BW, et al. Different perfusion pattern between acute and chronic pulmonary thromboembolism: evaluation with two-phase dual-energy perfusion CT. *AJR Am J Roentgenol* 2013;200:812-817
30. Iyer KS, Newell JD Jr, Jin D, Fuld MK, Saha PK, Hansdottir S, et al. Quantitative dual-energy computed tomography supports a vascular etiology of smoking-induced inflammatory lung disease. *Am J Respir Crit Care Med* 2016;193:652-661
31. Baxa J, Matouskova T, Krakorova G, Schmidt B, Flohr T, Sedlmair M, et al. Dual-phase dual-energy CT in patients treated with erlotinib for advanced non-small cell lung cancer: possible benefits of iodine quantification in response assessment. *Eur Radiol* 2016;26:2828-2836
32. Kim SJ, Lim HK, Lee HY, Choi CG, Lee DH, Suh DC, et al. Dual-energy CT in the evaluation of intracerebral hemorrhage of unknown origin: differentiation between tumor bleeding and pure hemorrhage. *AJNR Am J Neuroradiol* 2012;33:865-872
33. Tijssen MP, Hofman PA, Stadler AA, van Zwam W, de Graaf R, van Oostenbrugge RJ, et al. The role of dual energy CT in differentiating between brain haemorrhage and contrast medium after mechanical revascularisation in acute ischaemic stroke. *Eur Radiol* 2014;24:834-840
34. Jin KN, De Cecco CN, Caruso D, Tesche C, Spandorfer A, Varga-Szemes A, et al. Myocardial perfusion imaging with dual energy CT. *Eur J Radiol* 2016;85:1914-1921
35. Hur J, Kim YJ, Lee HJ, Nam JE, Hong YJ, Kim HY, et al. Cardioembolic stroke: dual-energy cardiac CT for differentiation of left atrial appendage thrombus and circulatory stasis. *Radiology* 2012;263:688-695
36. Ascenti G, Mazziotti S, Lamberto S, Bottari A, Caloggero S, Racchiusa S, et al. Dual-energy CT for detection of endoleaks after endovascular abdominal aneurysm repair: usefulness of colored iodine overlay. *AJR Am J Roentgenol* 2011;196:1408-1414
37. Goo HW, Chae EJ, Seo JB, Hong SJ. Xenon ventilation CT using a dual-source dual-energy technique: dynamic ventilation abnormality in a child with bronchial atresia. *Pediatr Radiol* 2008;38:1113-1116
38. Chae EJ, Seo JB, Goo HW, Kim N, Song KS, Lee SD, et al. Xenon ventilation CT with a dual-energy technique of dual-source CT: initial experience. *Radiology* 2008;248:615-624
39. Park EA, Goo JM, Park SJ, Lee HJ, Lee CH, Park CM, et al. Chronic obstructive pulmonary disease: quantitative and visual ventilation pattern analysis at xenon ventilation CT performed by using a dual-energy technique. *Radiology* 2010;256:985-997
40. Chae EJ, Seo JB, Lee J, Kim N, Goo HW, Lee HJ, et al. Xenon ventilation imaging using dual-energy computed tomography in asthmatics: initial experience. *Invest Radiol* 2010;45:354-361
41. Goo HW, Yu J. Redistributed regional ventilation after the administration of a bronchodilator demonstrated on xenon-inhaled dual-energy CT in a patient with asthma. *Korean J Radiol* 2011;12:386-389
42. Kim WW, Lee CH, Goo JM, Park SJ, Kim JH, Park EA, et al. Xenon-enhanced dual-energy CT of patients with asthma: dynamic ventilation changes after methacholine and salbutamol inhalation. *AJR Am J Roentgenol* 2012;199:975-981
43. Goo HW, Yang DH, Hong SJ, Yu J, Kim BJ, Seo JB, et al. Xenon ventilation CT using dual-source and dual-energy technique in children with bronchiolitis obliterans: correlation of xenon and CT density values with pulmonary function test results. *Pediatr Radiol* 2010;40:1490-1497
44. Goo HW, Yang DH, Kim N, Park SI, Kim DK, Kim EA. Collateral ventilation to congenital hyperlucent lung lesions assessed on xenon-enhanced dynamic dual-energy CT: an initial experience. *Korean J Radiol* 2011;12:25-33
45. Honda N, Osada H, Watanabe W, Nakayama M, Nishimura K, Krauss B, et al. Imaging of ventilation with dual-energy CT during breath hold after single vital-capacity inspiration of stable xenon. *Radiology* 2012;262:262-268
46. Goo HW. Dual-energy lung perfusion and ventilation CT in children. *Pediatr Radiol* 2013;43:298-307
47. Yoon SH, Goo JM, Jung J, Hong H, Park EA, Lee CH, et al. Computer-aided classification of visual ventilation patterns in

patients with chronic obstructive pulmonary disease at two-phase xenon-enhanced CT. *Korean J Radiol* 2014;15:386-396
48. Hachulla AL, Pontana F, Wemeau-Stervinou L, Khung S, Faivre JB, Wallaert B, et al. Krypton ventilation imaging using dual-energy CT in chronic obstructive pulmonary disease patients: initial experience. *Radiology* 2012;263:253-259
49. Hong SR, Chang S, Im DJ, Suh YJ, Hong YJ, Hur J, et al. Feasibility of single scan for simultaneous evaluation of regional krypton and iodine concentrations with dual-energy CT: an experimental study. *Radiology* 2016;281:597-605
50. Qu M, Ramirez-Giraldo JC, Leng S, Williams JC, Vrtiska TJ, Lieske JC, et al. Dual-energy dual-source CT with additional spectral filtration can improve the differentiation of non-uric acid renal stones: an ex vivo phantom study. *AJR Am J Roentgenol* 2011;196:1279-1287
51. Li X, Zhao R, Liu B, Yu Y. Gemstone spectral imaging dual-energy computed tomography: a novel technique to determine urinary stone composition. *Urology* 2013;81:727-730
52. Coupal TM, Mallinson PI, Gershony SL, McLaughlin PD, Munk PL, Nicolaou S, et al. Getting the most from your dual-energy scanner: recognizing, reducing, and eliminating artifacts. *AJR Am J Roentgenol* 2016;206:119-128
53. Schulz B, Kuehling K, Kromen W, Siebenhandl P, Kerl MJ, Vogl TJ, et al. Automatic bone removal technique in whole-body dual-energy CT angiography: performance and image quality. *AJR Am J Roentgenol* 2012;199:W646-W650
54. Lee CW, Seo JB, Song JW, Kim MY, Lee HY, Park YS, et al. Evaluation of computer-aided detection and dual energy software in detection of peripheral pulmonary embolism on dual-energy pulmonary CT angiography. *Eur Radiol* 2011;21:54-62
55. Atak H, Shikhaliev PM. Dual energy CT with photon counting and dual source systems: comparative evaluation. *Phys Med Biol* 2015;60:8949-8975
56. Pourmorteza A, Symons R, Sandfort V, Mallek M, Fuld MK, Henderson G, et al. Abdominal imaging with contrast-enhanced photon-counting CT: first human experience. *Radiology* 2016;279:239-245
57. Yu Z, Leng S, Jorgensen SM, Li Z, Gutjahr R, Chen B, et al. Evaluation of conventional imaging performance in a research whole-body CT system with a photon-counting detector array. *Phys Med Biol* 2016;61:1572-1595